AGU PUBLICATIONS

JGR

Journal of Geophysical Research: Oceans

RESEARCH ARTICLE

10.1002/2016JC012079

Key Points:
- An ensemble of ocean reanalyses from 1815–2013 is described
- The reanalyses agree well with independent observations in the latter part of the record
- There is prominent variability of surface temperature, heat content and dynamic height

Correspondence to:
B. Giese,
b-giese@tamu.edu

Citation:
Giese, B. S., H. F. Seidel, G. P. Compo, and P. D. Sardeshmukh (2016), An ensemble of ocean reanalyses for 1815–2013 with sparse observational input, *J. Geophys. Res. Oceans*, *121*, 6891–6910, doi:10.1002/2016JC012079.

Received 21 JUN 2016
Accepted 12 AUG 2016
Accepted article online 18 AUG 2016
Published online 21 SEP 2016

An ensemble of ocean reanalyses for 1815–2013 with sparse observational input

Benjamin S. Giese[1], Howard F. Seidel[1], Gilbert P. Compo[2,3], and Prashant D. Sardeshmukh[2,3]

[1]Department of Oceanography, Texas A&M University, College Station, Texas, USA, [2]CIRES, University of Colorado, Boulder, Colorado, USA, [3]Division of Physical Sciences, NOAA Earth Systems Research Laboratory, Boulder, Colorado, USA

Abstract This paper describes a new eight-member ensemble of ocean reanalyses spanning nearly 200 years from 1815 to 2013 generated using the Simple Ocean Data Assimilation system with sparse observational input (SODAsi) to explore long-term changes in the oceans. The eight ensemble members assimilate surface temperature observations and use surface boundary conditions from an atmospheric reanalysis that is loosely coupled to the ocean reanalysis. Both surface and subsurface quantities, such as dynamic height and heat content, show a broad spectrum of variability. Surface temperature trends from 1815 to 2013 are positive in most regions, with some important exceptions; the central Tropical Pacific, around Antarctica, and in the Gulf Stream and Kuroshio extension regions all show cooling trends. A near-global average shows warming of about 0.8°C over the full period, with most of the warming occurring after 1920. There is pronounced multidecadal variability in both the midlatitude and tropical oceans. In the North Atlantic Ocean, temperature variability is highly correlated with the meridional overturning stream function, with the largest correlation occurring when the stream function is advanced by 9 years. Trends of upper ocean heat content and dynamic height from the 1950s onward compare well with previously published values. Globally averaged heat content of the upper 700 m shows a nearly linear rise after the 1920s, requiring a net downward surface heat flux increase of 0.47 W m^{-2} into the ocean. This is close to published estimates of the increased flux required to explain the heat content increase from 1971 to 2010.

1. Introduction

The response of the climate system, especially that of global mean surface temperature, to increasing greenhouse gases in the atmosphere has been analyzed in a variety of ocean-atmosphere coupled climate models [*Meehl et al.*, 2007]. Understanding this response is important for understanding anthropogenic climate change and for improving climate predictions. There is a pressing need to validate the coupled climate models used for making predictions, so that scientists and policymakers understand their benefits and limitations. Unfortunately, because few subsurface ocean observations were made before the late 1960s, validations of oceanic changes are often restricted to those of sea surface temperature (SST).

To address the need for long-term SST records, several "reconstructed" SST data sets have been developed. Spatially and temporally complete global data sets such as Kaplan SST v2 [*Kaplan et al.*, 1998], HadISST 1.1 (Hadley Centre Sea Ice and SST, version 1.1) [*Rayner et al.*, 2003], and ERSST v4 (Extended Reconstructed SST, version 4) [*Huang et al.*, 2015] are based on statistical interpolation techniques to reconstruct the SST field. A drawback of these reconstructions is that they use recent patterns of climate variability in periods of dense observations to estimate patterns of variability in earlier periods of sparse observations. This assumes that the structure of climate variability in the earlier periods was similar to that in recent periods. However, as shown by *Giese and Ray* [2011], the structure of important aspects of climate variability such as the El Niño Southern Oscillation (ENSO) phenomenon varies considerably in time, raising the possibility that traditional methods to reconstruct SST fields do not capture the full range of the actual variability.

An alternative approach is to combine observations with model-generated estimates through the process of data assimilation [*Daley*, 1991; *Kalnay*, 2003]. Algorithms have been developed to optimally merge sparse observational data with guesses generated using state-of-the-art numerical models to provide estimates of time evolving atmospheric and oceanic states. When used to estimate the state (an "analysis") of a geophysical system in retrospect, such approaches are termed "reanalysis."

A central concern with reanalysis data sets of sparsely observed periods is how they differ from a model simulation. This was the subject of a series of experiments conducted at Texas A&M University and reported by *Carton et al*. [2012]. In those experiments, observations for 1995–1998 were degraded to the observation densities of 1925–1928, 1945–1948, and 1965–1968. No meaningful impact of hydrographic observations was found before the late 1960s, but SST observations have an impact even for the sparse density of 1925–1928. A second set of experiments was conducted by degrading the atmospheric forcing within the error bars estimated from the 20CRv2 (20th Century Reanalysis version 2, *Compo et al*. [2011]) reanalysis. These experiments show that if the historical representation of surface meteorological forcing is sufficiently accurate (if we accept the 20CRv2 error estimates) then tropical phenomena of the magnitude of the 1997/1998 El Niño and associated 1997 Indian dipole and 1998 La Niña could be described qualitatively at least as early as the 1920s and likely even earlier.

Reanalyses are useful for providing a long-term perspective on climate change. In this context it is notable that *Ray and Giese* [2012] found no statistically significant trends from 1871 to 2008 in an oceanic reanalysis data set (SODA 2.2.4) in the strength, frequency, duration, location, or direction of propagation of El Niño and La Niña events. Their finding, however, has an important caveat that the surface forcing in SODA 2.2.4 was specified using the ensemble mean fields from the ensemble of atmospheric 20CRv2 reanalyses. This averages out the high-frequency wind stress variability in periods of sparse observations. The effect is greater in the early part of the record when the few atmospheric observations do not adequately resolve the high-frequency forcing.

Resolving the high-frequency component of the forcing can have an important impact on estimates of low-frequency climate variability. For example, *Yang and Giese* [2013] found the structure of ENSO is different in model integrations using ensemble mean forcing (as was used for SODA 2.2.4) compared to integrations using individual member forcing. They attributed this to the fact that in the western Pacific, higher-frequency components of the forcing substantially enhance evaporation and contribute to cooler SST. This contribution acts to weaken the mean zonal SST gradient, and thus to weaken the amplitude of ENSO in the western Pacific. Interestingly, *Yang and Giese* [2013] also found that using the individual member forcing can strengthen ENSO in the eastern Pacific, because the stronger winds generate stronger oceanic Kelvin waves that propagate to the eastern Pacific region of the shoaling thermocline.

In this paper, we explore an ensemble of oceanic reanalyses generated using individual members of an ensemble of atmospheric forcing fields derived from an updated experimental version of the atmospheric 20th century reanalysis system. We are chiefly motivated by the need to improve the characterization of oceanic variability in the 19th to the mid-20th centuries, especially in relation to that of the better-observed more recent period.

2. Methods

The new reanalyses use the Simple Ocean Data Assimilation (SODA) methodology [*Carton and Giese*, 2008] comprising the Parallel Ocean Program (POP) [*Smith et al*., 1992] ocean model and SODA algorithm. Several previous versions of SODA spanning the 20th century [*Giese et al*., 2010; *Giese and Ray*, 2011; *Ray and Giese*, 2012] used ensemble mean atmospheric forcing from the 20th Century Reanalysis [*Compo et al*., 2011]. As discussed by *Yang and Giese* [2013], relying on ensemble mean forcing is acceptable in times of numerous observations but can generate large biases in times of few observations because the weather noise is averaged out in times of few observations. In this paper, we describe a new version of SODA (SODAsi.3 where si stands for sparse input) generated using individual ensemble members of atmospheric forcing fields from a newer version of the 20th Century Reanalysis data set.

The SODA system has been described in detail elsewhere [*Carton and Giese*, 2008]. Briefly, the POP ocean model is used with a horizontal resolution of 0.4° (zonal) × 0.25° (meridional) and 40 vertical levels with 10 m spacing near the surface. The model covers the global domain with a distorted grid in the Northern Hemisphere to allow for a displaced North Pole in order to adequately resolve the Arctic Ocean. The meridional resolution increases poleward to reduce the grid anisotropy that results from the Mercator coordinate grid due to the convergence of meridians at high latitudes. K-profile parameterization is used for vertical mixing, and biharmonic diffusion is used for horizontal mixing. River input is included with climatological

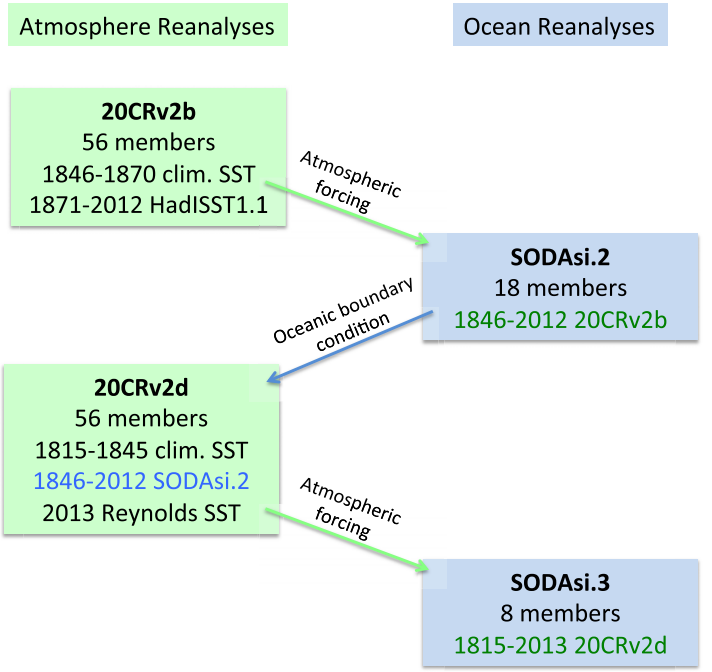

Figure 1. Coupling strategy used to produce SODAsi.3. Experiments are described in the text. The years for the 20CR system using specified SST source fields are indicated in the left hand plots. The right hand plots indicate the span of years in the subsequent SODAsi version.

seasonal discharge. There is no explicit sea ice model; however the surface heat flux is modified when the surface temperature reaches the freezing point of seawater.

In the SODAsi.3 system presented here, many elements of the SODA system are retained. The major difference is that only SST observations, contained in the International Comprehensive Ocean-Atmosphere Data Set [ICOADS *Woodruff et al.*, 2010] version 2.5, are assimilated, applying the spatially and monthly varying bucket corrections used in HadISST 1.1 [*Rayner et al.*, 2003] to the ICOADS observations. In contrast, all available surface and subsurface temperature and salinity observations were used in previous versions of SODA. Our main motivation for not using the subsurface temperature and salinity profile data in SODAsi.3 is to avoid generating spurious decadal climate variability due to the rapidly increasing density of hydrographic measurements after the 1950s.

Observations are assimilated in a sequential 10 day update cycle, with the model guess error covariances specified from a simulation without assimilation. The assimilation cycle operates as follows. A 5 day simulation from day t to day t+5 is generated first. At day t+5, an analysis is performed to produce an estimate of the ocean state, using observations within 45 days of the analysis date. Innovations are calculated as the difference between the analysis and the first guess. Although only SST is assimilated, the covariance between salinity and temperature is used to estimate salinity innovations, because updating only temperature creates spurious water masses [*Carton and Giese*, 2008]. For salinity there is a damping to climatology during the model integration with a time scale of 5 years. The model is restarted at day t and integrated to day t+10 with temperature and salinity innovations added incrementally at every time step. At day t+10, the procedure is repeated. The model generated 5 day averages are mapped onto a uniform global 0.5° × 0.5°horizontal grid using the spherical coordinate remapping and interpolation package of *Jones* [1999].

An important new feature of the SODAsi.3 system is its use of a "loosely coupled" ocean-atmosphere framework to extend the reanalyses back to 1815. The loose coupling refers to alternating iterations of the SODAsi and 20CR assimilations using boundary forcing from previous iterations, specifically a SODAsi.2 assimilation followed by a new 20CR assimilation and then by SODAsi.3, as depicted schematically in Figure 1. The left-hand column of Figure 1 shows the two atmospheric reanalyses (20CRv2b and 20CRv2d) and the right-hand column shows the two ocean reanalyses (SODAsi.2 and SODAsi.3) that were generated. The iterative coupling proceeds from the top of the figure to the bottom of the figure. In lieu of full coupling, such a loose coupling attempts to improve the mutual consistency of the atmospheric and oceanic assimilations.

For the first iteration of this loosely coupled reanalysis, the 18 ensemble members of SODAsi.2 use boundary conditions from 20CRv2 for the 1948 to 2012 period, and from an experimental version of 20CR (20CRv2ex) that assimilates additional pressure observations [*Cram et al.*, 2015] for the earlier 1846–1947 period. We refer to this combined 20CR version as 20CRv2b. The lower boundary conditions of SST and sea ice concentration for 20CRv2 are from the UK Met Office HadISST 1.1 data set [*Rayner et al.*, 2003] interpolated from monthly to daily resolution. For the 1871–1947 period, 20CRv2b also used HadISST 1.1, but for

earlier periods the monthly HadISST 1.1 monthly climatology of 1871–1900 is prescribed. Because of a spectral pattern in the surface wind stress from 20CRv2 [*Kent et al*., 2012], the surface wind stress average from 1979 to 2008 is removed and replaced by the ERA-interim [*Dee et al*., 2011] mean wind stress averaged over the same period.

For the second iteration of the coupled system (see Figure 1), three experiments using the 20CR methodology are combined to provide surface boundary conditions for SODAsi.3. We call this combination 20CRv2d. The first segment extends from 1815 to 1930. Before 1846 this segment uses SST from an SST climatology derived from the COBE v2 data set for the 1861–1890 period. From 1846 to 1930, the segment uses SST from SODAsi.2. The second segment of 20CRv2d spans the 1931–2012 period. This segment is the same as 20CRv2c, which also uses SODAsi.2 for SST boundary conditions. The third segment is for the year 2013, and this piece specifies SST from OISST v2 [*Reynolds et al*., 2007]. All segments specify sea ice concentrations from the COBE v2 data set [*Hirahara et al*., 2014], with its 1861–1890 climatology specified before 1851.

Surface wind stresses from 20CRv2b and 20CRv2d are used for computing surface momentum fluxes and solar radiation, specific humidity, cloud cover, 2m air temperature, precipitation, and 10 m-wind speed are used for computing heat and freshwater fluxes. Daily averages are used as boundary conditions. All ensemble members of the ocean reanalyses use the same ocean observations and assimilation system. The chief benefit of generating such an ensemble of reanalyses is that it provides a measure of uncertainty in the reanalyzed oceanic fields and in other fields derived from them, such as monthly or annual averages used to study climate variability and change.

The atmospheric model used for 20CRv2b and 20CRv2d is the same as for 20CRv2 and is described by *Compo et al*. [2011]. It is a coupled atmosphere-land model based on the NCEP Global Forecast System (GFS) with a horizontal resolution of 62 spherical wavenumbers (T62) and a vertical resolution of 28 hybrid sigma-pressure levels. An 11 year solar cycle, time-varying CO2 concentrations and volcanic aerosols are prescribed [*Compo et al*., 2011]. Volcanic aerosols after 1850 are prescribed using estimates of *Sato et al*. [1993]. Prior to 1851 volcanic aerosol estimates of *Crowley and Unterman* [2013] are used.

For surface pressure observations, three different versions of the International Surface Pressure Databank (ISPD) [*Cram et al*., 2015, *Compo et al*., 2011] are used. 20CRv2 only assimilates surface and sea level pressure observations from ISPD version 2. The observations in ISPD come from land stations, marine observations, and tropical cyclone "best track" pressure observations and reports. Sea Level Pressure (SLP) from the ICOADS marine observations is provided by ICOADS 2.4 for the period of 1952–2008 and by ICOADS 2.5 for the period of 1846–1951. Tropical cyclone data are provided by the International Best Track Archive for Climate Stewardship (IBTrACs). As described by *Compo et al*. [2011], extensive quality control procedures are conducted on ISPD observations before assimilating the pressure observations. For the period 1846–1948, ISPD version 3 is used to generate 20CRv2ex. This version includes many additional observations over land and ocean. Differences are described by *Cram et al*. [2015] and include pressure observations from hundreds of new stations around the world and thousands of newly recovered marine SLP observations from ships of exploration during the mid-19th to mid-20th centuries [*Allan et al*., 2011].

For 20CRv2d, surface pressure observations for 1815–1930 from the newly assembled ISPD version 4 were used *Cram et al.* [2015]. This version incorporates new station and marine observations during the early 19th to early 20th centuries from several ongoing digitization efforts by previous contributors to the ISPD [*Cram et al*., 2015], and also incorporates new contributions facilitated by the Atmospheric Circulation Reconstructions over the Earth Initiative [*Allan et al*., 2011], including the citizen-science efforts of Oldweather.org and WeatherDetective.org, the international efforts of the ERA-CLIM project [*Stickler et al*., 2014], and extensive digitizations for stations back to 1815 [*Brugnara et al*., 2015].

The assimilation procedure for the new versions of 20CR used for SODAsi is the same as for previous versions: an Ensemble Kalman Filter algorithm based on an ensemble square root filter [*Whitaker and Hamill*, 2002; *Whitaker et al*., 2004, *Compo et al*., 2006; *Compo et al*., 2011]. For each 6 hourly analysis, an ensemble of 56 9 hour "first guess" forecasts was generated and 56 6 hourly analyses were produced. 20CRv2 is the first synoptic reanalysis data set extending back into the 19th century of very sparse observations, which also provides estimates of the analysis uncertainty at each analysis time as the ensemble standard deviation. Extensive comparisons with independent observations such as radiosonde data, numerical weather prediction (NWP) forecasts, atmospheric reanalyses using all available observations, and statistical climate

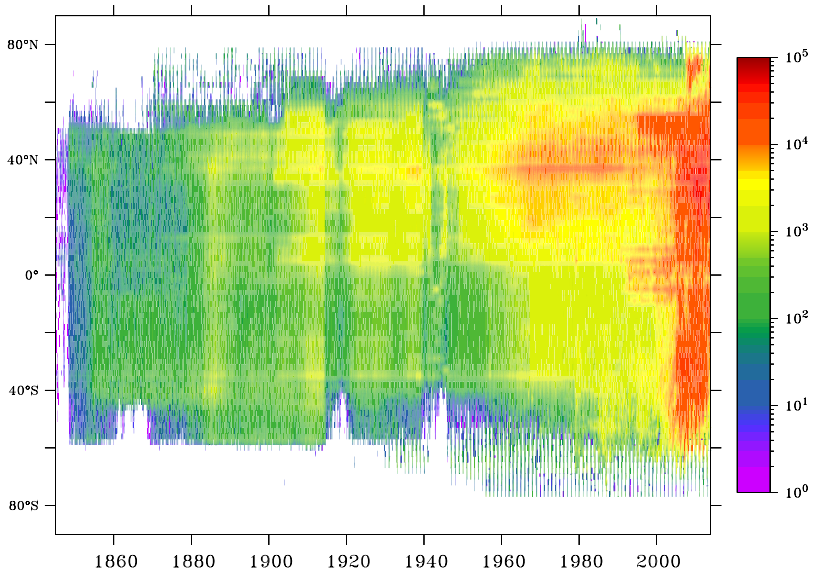

Figure 2. Time-latitude distribution of the number of SST observations each month in different latitude bands in the ICOADS 2.5 data set. Note that the key represents a log scale.

reconstructions have demonstrated that 20CRv2 accurately captures, within its estimated error bars, much of the observed weather and climate variability [*Compo et al*., 2011; *Brönnimann et al*., 2011, 2012; *Compo et al*., 2013], including hydroclimatic variability [*Greve et al*., 2014].

3. Results

An important aspect of this work is to estimate uncertainty in the reanalysis fields. To address uncertainty, we explore some properties of the observations used by SODAsi.2 and some properties of the prescribed 20CRv2b surface wind forcing. We use SODAsi.2 for this section because there are 18 ensemble members in that experiment, as opposed to 8 in SODAsi.3. The variance and the ensemble spread are the same for the two experiments in the period for which they overlap (not shown). The latitudinal distribution of ICOADS 2.5 observations is illustrated in Figure 2. Similar figures for the distribution of surface pressure observations used by the 20CR system are presented by *Cram et al*. [2015]. The figure shows the zonally averaged number of observations as a function of latitude for the period from 1850 to the present.

There are few ocean observations digitally available anywhere before 1880. The number of observations increases in the last decades of the 1800s, mostly because of measurements in the Atlantic Ocean, along transects between Europe and the United States, and between Europe and South America. Figure 2 also shows a noticeable hemispheric bias in the number of observations throughout the record, with more Northern than Southern Hemisphere observations until the start of the 21st century. This bias is largest in the latter half of the 20th century when many of the oceanographic and shipping observations were made in the North Atlantic and North Pacific Oceans. There are also noticeable decreases during the two World Wars, from around 1914–1920 and again in the early 1940s.

Despite the sparseness of observations in the late 1800s and early 1900s, *Carton et al*. [2012] show that these observations, in conjunction with an atmospheric reanalysis that uses surface pressure observations, can resolve much of the structure and evolution of ENSO. Current data rescue initiatives may improve upon the sparseness of surface observations in future releases [*Allan et al*., 2011; *Woodruff et al*., 2010]. The number of SST observations in the midlatitude northern oceans is much improved in the late 1950s (associated with the International Geophysical Year), and the northern oceans remains relatively well observed to the present, however the rest of the global oceans remain poorly observed until the end of the 20th Century. The introduction of the TOGA-TAO observing array in the 1990s increased the number of observations in the tropical Pacific, but it is not until the deployment of the Argo network of profiling floats in the early 2000s that coverage in the Southern Ocean becomes comparable to that in the rest of the global oceans.

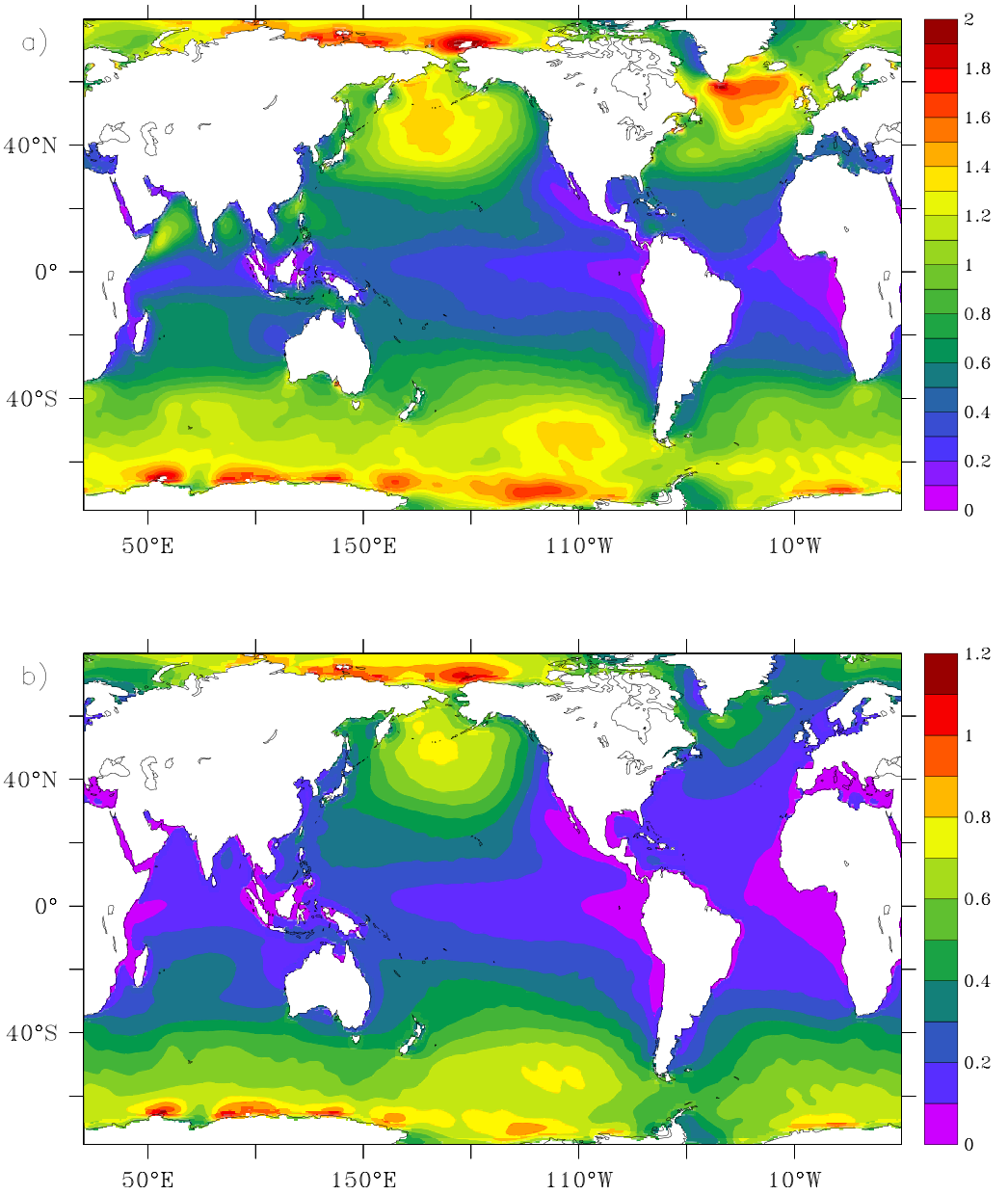

Figure 3. (a) The temporal standard deviation of 5 day mean zonal wind stress (N m^{-2}) calculated using the 18 ensemble members of 20CRv2b used by SODAsi.2. The standard deviation is calculated from 1871 to 2011. (b) The time average of the ensemble spread of 5 day mean zonal wind stress from the 18 members.

In addition to uncertainty introduced by the changing observation density, uncertainty is introduced via the surface boundary conditions. Figure 3a shows the standard deviation of the 5-day mean zonal wind stress from 20CRv2b averaged over the 18 ensemble members used by SODAsi.2. As expected, variability is large at high latitudes, and small in the tropics. The ensemble spread, taken here to be the RMS (Root Mean Square) of differences from the ensemble mean, is shown in Figure 3b and has a pattern similar to that of Figure 3a, with high ensemble spread associated with regions of high variability. Interestingly, the ensemble spread in the North Atlantic Ocean is considerably smaller than in the North Pacific Ocean, despite the larger variance in the North Atlantic Ocean. This can be explained by the greater number of observations acting to reduce the ensemble spread, particularly in the early part of the record, in the North Atlantic Ocean [*Compo et al.*, 2011].

Given that the observational density in 20CRv2b is time-dependent, the ensemble spread is also time-dependent. This is illustrated in Figure 4a, which shows the globally averaged standard deviation of the 5

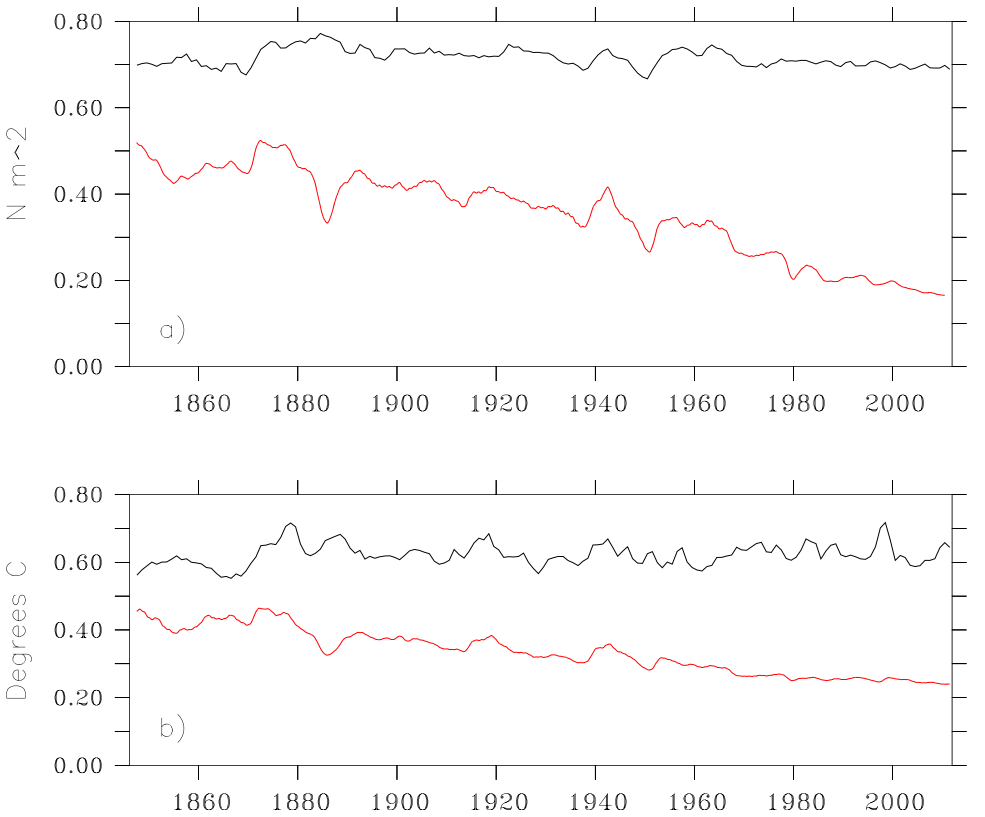

Figure 4. The temporal distribution of the standard deviation (black line) and ensemble spread (red line) of (a) zonal wind stress in N m^{-2} averaged over the ocean from 20CRv2b and (b) SST from SODAsi.2. The standard deviation is calculated using a 3 year moving window and is averaged over the 18 members used in SODAsi.2.

day zonal wind stress (black line) and ensemble spread (red line), calculated in 3 year windows. In the late 1800s, the ensemble spread is reasonably similar to the temporal standard variation. However, as the number of observations increases throughout the 20th century, the intrinsic variability remains at approximately the same level of about 0.7 N m^{-2}, whereas the ensemble spread decreases to about 0.20 N m^{-2}.

Uncertainty in the surface wind stress fields translates to uncertainty in SST in SODAsi.2. Figure 5 shows the standard deviation and ensemble spread of 5 day averaged SST, also calculated using all data from 1871 through 2011. As expected, SST variability is largest in the northwestern Pacific and North Atlantic Oceans, in the Southern Ocean from about 20°S to the Antarctic coast, and in the eastern equatorial Pacific and Atlantic Oceans. Other than in the eastern Pacific and Atlantic regions, most of the tropical oceans have relatively little SST variability. By way of comparison, the ensemble spread (Figure 5b) reflects some of the regions for which there is largest intrinsic ocean variability: the western boundary extension regions in the Atlantic and Pacific Oceans; in the eastern tropical Pacific; and along the Antarctic Circumpolar Current front. Interestingly, there is also a region of higher than average spread in the high latitude North Atlantic Ocean, between Greenland and Norway. In the eddy region associated with the Antarctic Circumpolar Current, there is modest SST variability, but large ensemble spread, suggesting that individual ensemble members have eddies in different positions in these sparsely observed regions.

Although one expects SST variability to remain relatively stable through time, the same need not be true of the ensemble spread, given the changes in observation density in both the atmosphere and ocean. SODAsi.2 SST reflects this expectation. The global ocean average of the temporal standard deviation of SST is indeed relatively constant at about 0.6°C (Figure 4b). In contrast, the ensemble spread decreases from about 0.45°C at the start of the record to about 0.25°C at the end of the record. There are some interesting fluctuations in this downward trend. Notably, there is a brief period of lower spread in the 1880s, associated with an increase in observations (mostly from the U.S. Marine Meteorological Journals Collection, [*Woodruff et al.*, 2010]), and increased spread during the two World Wars when fewer observations are available.

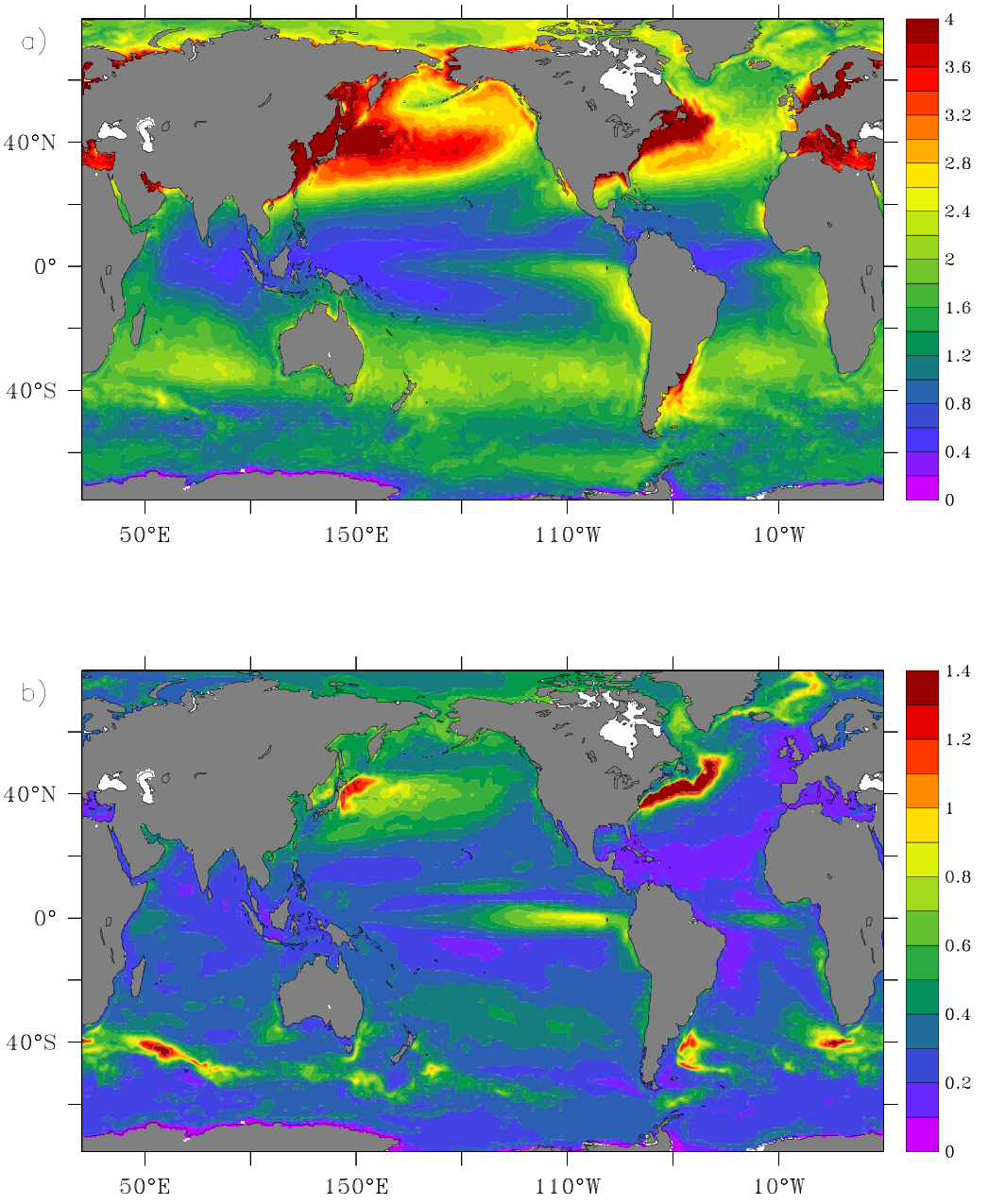

Figure 5. (a) The standard deviation of 5 day mean SST (°C) averaged over the 18 ensemble members in SODAsi.2 (contour interval 0.2°C). The standard deviation is calculated from 1871 to 2011. (b) The time average of the ensemble spread of 5 day mean SST from the 18 ensemble members (shading interval 0.1°C). Note differences in the scales.

A final methodological question is how many ensemble members are needed to represent SST variability in the reanalyses. To address this issue, we explore the number of ensemble members needed to represent SST in a different SST data set, in this case ERSST v4. We show in Figure 6 SST at 140°W and the equator for 1960–1969 from SODAsi.2 and from ERSST v4 [*Huang et al.*, 2015]. We choose this time period and location because there are some, but not many observations during this time, and this location has a large ensemble spread to temporal standard deviation ratio (compare Figures 4a and 4b). Clearly there is considerable spread between the ensemble members. For the most part, the ensemble members bracket the estimate from ERSST v4, although there are times (such as in 1962 and 1968) when ERSST v4 falls outside of the ensemble of estimates.

In Figure 7, we show the RMS difference between an ensemble average composed of 1 through all 18 ensemble members and the ERSST v4 SST estimate. Using just one ensemble member results in an RMS

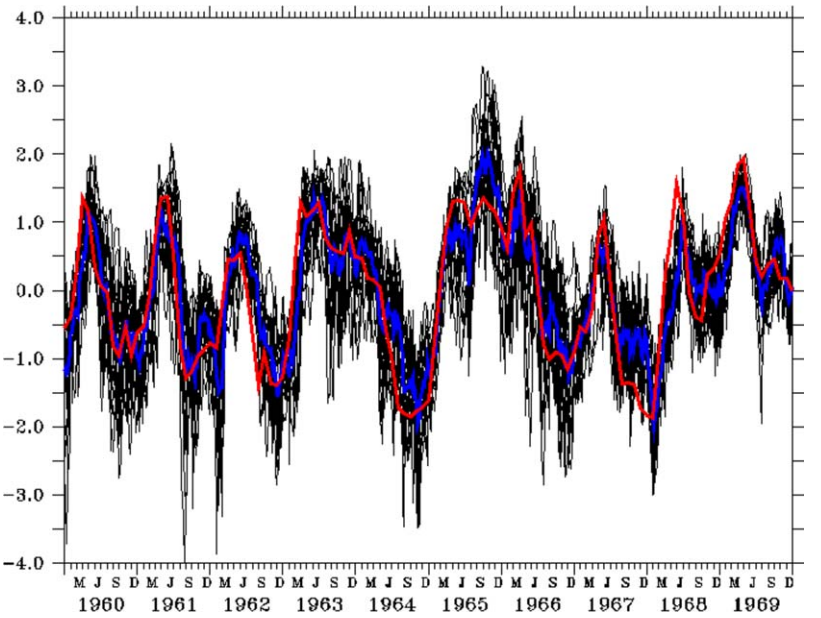

Figure 6. Time series of SST at 140°W and the equator for the 18 ensemble members of SODAsi.2 (black), the ensemble average from SODAsi.2 (blue), and from ERSST v4 (red).

difference of just over 0.66°C. However, using additional ensemble members quickly reduces this RMS difference, flattening out at a value of about 0.54°C. After approximately eight ensemble members, including additional members does not markedly reduce the difference between the ensemble mean and ERSST v4. A similar analysis using other reconstructed SST products produces a similar result (not shown). Based on these results, and the constraints of available computational resources, we elected to use eight ensemble members for SODAsi.3.

3.1. Global Quantities

As an illustration of the new information available in SODAsi.3, using one of the ensemble members we show the 5 day averaged evolution of the 1877/1878 El Niño event. All ensemble members have westerly wind bursts and warm El Niño SSTs, but differ in their details. The ensemble member chosen (#8) was chosen subjectively to show that the reanalysis captures both high and low-frequency characteristics of ENSO. This event has been long suspected of being a major El Niño event [*Kiladis and Diaz*, 1986, *Quinn et al.*, 1987], but only sparse observations are available for this period (e.g., Figure 2). Therefore, many details of

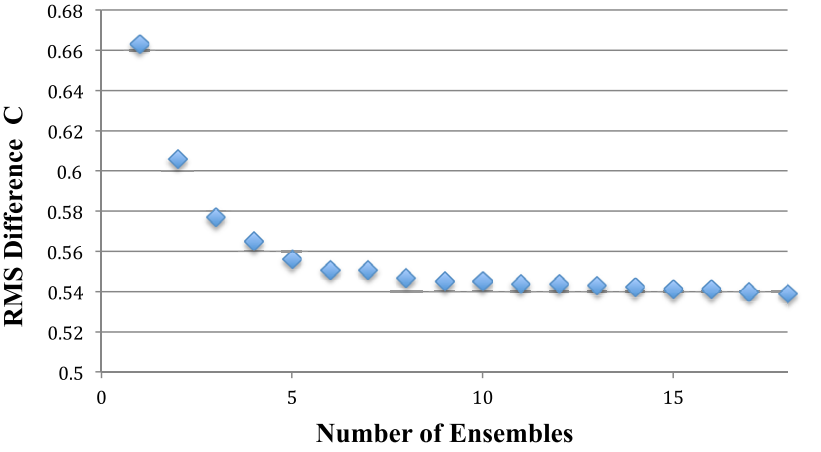

Figure 7. Blue diamonds show the RMS difference between SST from ERSST v4 a mean constructed from 1 to 18 ensemble members from SODAsi.2 and SST at 140°W and the equator for the period from 1960 through 1969.

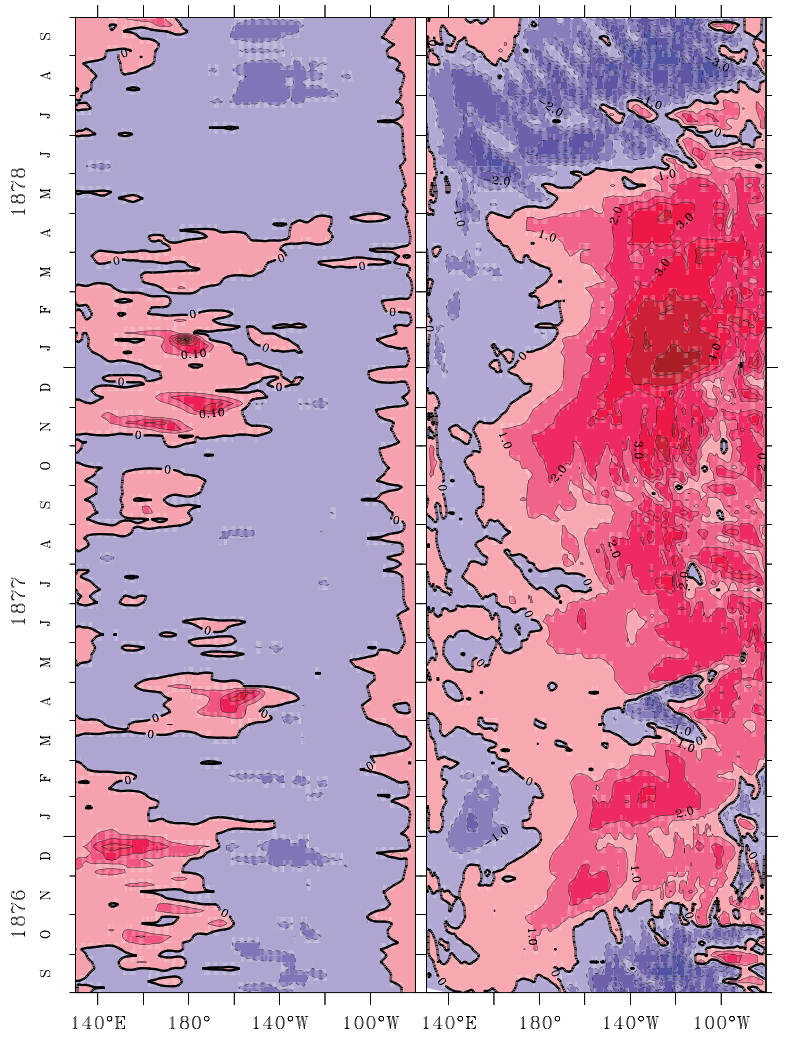

Figure 8. (left) Zonal wind stress(contour interval 0.5 N m^{-2}) and (right) SST anomaly (contour interval 1.0°C) from Ensemble member #08 of SODAsi.3. Both wind stress and SST have been averaged over 5 day intervals. Note the episodes of westerly wind stress and their relationship to warming in the east.

how this event developed are not well known. By consistently combining the dynamical atmospheric information from the 20CRv2d, the ocean model, and the available SST observations, the SODAsi.3 improves upon this situation. The left hand plot of Figure 8 shows a series of westerly wind anomalies, as represented in zonal wind stress, from October 1876 through July 1877. These wind anomalies excite a strong Kelvin wave response [*Giese and Harrison*, 1990] that induces a strong warming signal in the eastern equatorial Pacific (Figure 8, right). When the easterlies strengthen in 1878 there is a rapid termination of the warm anomalies, and drives the formation of tropical instability waves that are apparent in the SST record. For the first time, estimates of the 3-dimensional ocean state associated with variability such as this event can be compared to modern events such as in 1997/1998 and 2015/2016.

With this new data set, we can now examine ocean variability and trends. To begin, we turn our attention to some indices of ocean structure. For this part of the analysis, we use monthly averaged values. Figure 9 shows the near global (60°S–60°N ocean average) SST from the eight ensemble members of SODAsi.3 and from three widely used SST reconstructions (HadISST 1.1 [*Rayner et al*. 2003], ERSSTv4 [*Huang et al*., 2015], and COBE v2 [*Hirahara et al*. 2014]). Each ensemble member from SODAsi is shown as a thin black line. Because these are averaged in time over a month and averaged in space globally, differences between the ensemble members are largely averaged out, and individual lines are difficult to resolve. Overall there is excellent agreement between SODAsi.3 and HadISST 1.1. All of the SST products rely on a similar set of

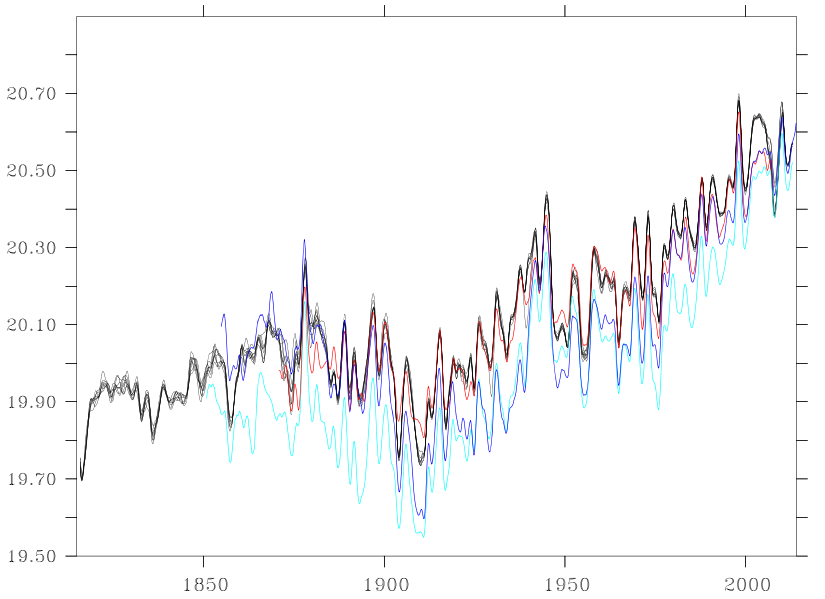

Figure 9. SST averaged from 60°S to 60°N for the eight SODAsi.3 ensemble members (shown as thin black lines) and from HadISST 1.1 (red line), ERSSTv4 (dark blue line), and COBE v2 (cyan line). All data sets have been smoothed with a 23 month Parzen filter.

observations, and SODAsi.3 and HadISST 1.1 use the same bucket corrections, so it is not too surprising that there is overall agreement. Examining the time series in some detail, there is a period of cooling from 1880 through about 1910, warming from 1910 through the early 1940s, possibly a weak cooling from the 1940s through the mid-1970s, and then continued warming from about 1980 to the end of the record. All four products agree with these overall patterns.

There are some prominent differences between the three reconstructions, particularly in the early 20th century, with ERSST and COBE v2 generally cooler than HadISST 1.1. This difference is most pronounced in the early to mid-1900s, with both about 0.2°C cooler than HadISST 1.1. Much of this difference, but not all of it, can be attributed to different approaches to the bucket correction [*Rayner et al*., 2003]. Since SODAsi.3 uses the HadISST 1.1 bucket corrections, there tends to be much greater agreement between SODAsi.3 and HadISST 1.1 during the early 1900s. Importantly, SODAsi.3 has interannual variability before 1871, despite the fact that 20CRv2b is forced with a climatology of SST from HadISST. This interannual variability in SODAsi.3 (also present in ERSST and COBE) comes from observations in the ICOADS 2.5 data set, from surface pressure observations being used by 20CRv2b, and from coupling between SODAsi.2 and 20CRv2d. Note also that SODAsi.3 captures a cooling of about 0.2°C associated with the Tambora eruption in 1815.

To further examine the agreement, we present the correlation and the RMS difference between SODAsi.3 and the reconstruction fields (Table 1). The correlation and RMS difference is computed at each grid point using monthly values and then averaged zonally and from 60°S to 60°N. We also calculate the correlation and RMS difference of departures from the seasonal cycle and smoothed with a boxcar average of 12 months (shown in parentheses). The correlation is uniformly high, with a correlation coefficient that ranges between 0.87 for ERSST v4 and 0.89 for COBE v2. Much of this high correlation comes from the seasonal cycle, so we removed the seasonal cycle and averaged over 1 year. The correlations of anomalous SST range from 0.69 for ERSST v4 to 0.75 for COBE v2. The RMS differences also show good agreement between the products, with an RMS difference from 0.76 to 0.89°C including the seasonal cycle to between 0.67 and 0.77°C for anomalous SST.

Table 1. Comparison of SODAsi.3 Monthly Ensemble Mean SST and SST From HadISST 1.1, COBE v2, ERSSTv3b, and ERSST v4 for the Period From 1871 to 2012[a]

	Correlation	RMS Difference
HadISST 1.1	0.88 (0.70)	0.78 (0.67)
COBE v2	0.89 (0.75)	0.89 (0.73)
ERSST v3b	0.88 (0.70)	0.76 (0.74)
ERSST v4	0.87 (0.69)	0.80 (0.77)

[a]The correlation and RMS difference are calculated at each grid point and then averaged zonally and from 60°S to 60°N. Values with seasonal cycle removed and smoothed with a 12 month boxcar average are shown in parentheses.

An EOF (Empirical Orthogonal Functions) analysis of SST illustrates some of the patterns of variability

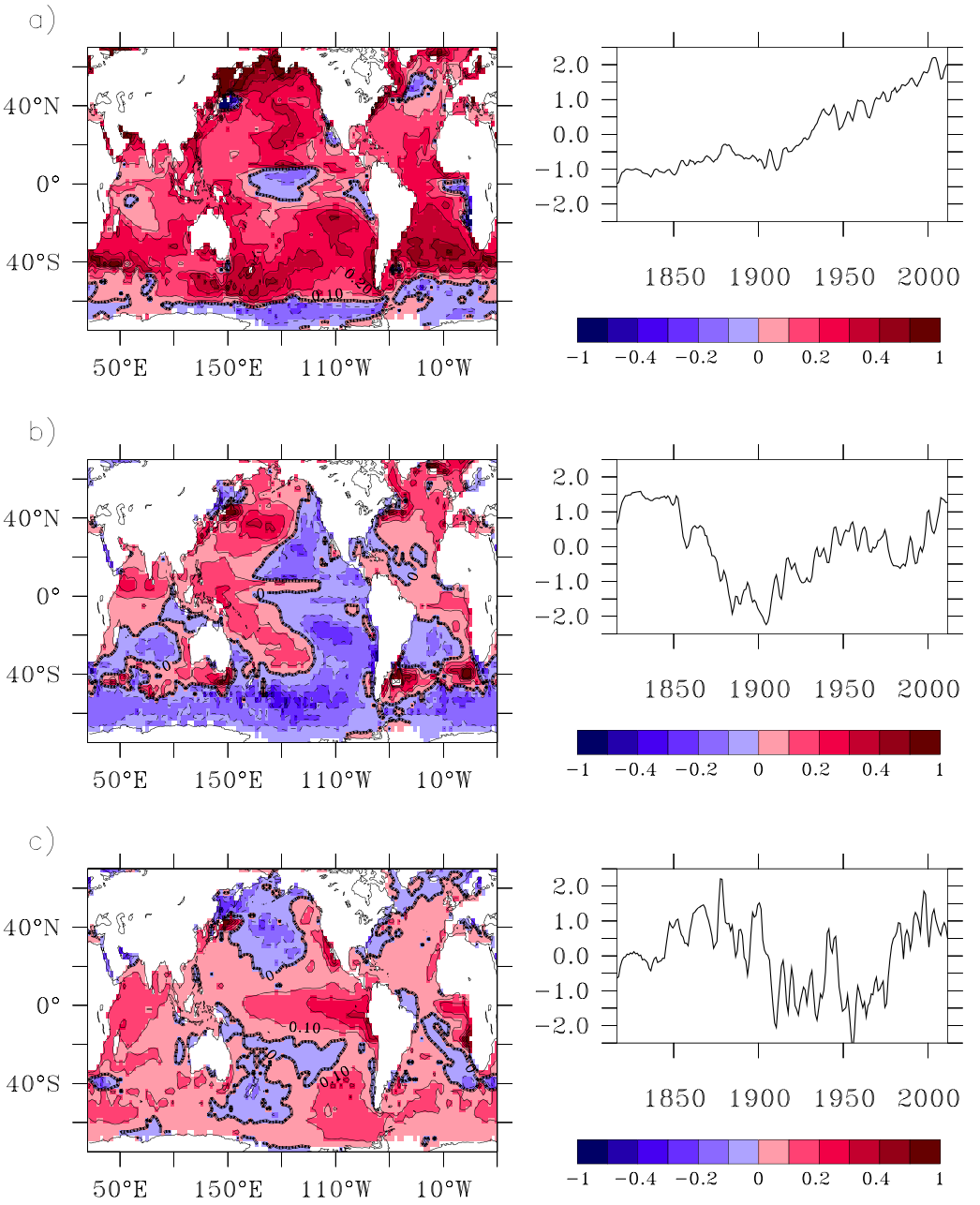

Figure 10. The first three EOFs of annually averaged SST anomalies in the 1871–2011 period. The (top) first, (middle) second, and (bottom) third EOFs explain 39%, 15%, and 7% of the total variance, respectively.

present in SODAsi.3. The EOF analysis is performed on annually averaged SST. The first EOF (Figure 10a) accounts for 39% of the total variance, and shows a nearly ubiquitous warming from about 1920 through the end of the record. Although the sign of SST change is mostly positive, there are some important spatial differences, and some regions that indicate cooling. Warming is strongest from 20°S to 60°S in the Southern Hemisphere, in the western boundary region of the North Atlantic extending up to the Labrador Sea, and in the central and high latitude North Pacific Ocean. There are also large values in the high latitude North Atlantic Ocean. Regions of cooling include poleward of 60°S along the coast of Antarctica, small regions in the central equatorial Pacific Ocean, in the eastern equatorial Pacific and Atlantic Oceans and in the Gulf Stream and Kuroshio extension regions. Cooling in the central Pacific was identified in an earlier SODA reanalysis but is not apparent in the CMIP5 historical runs [*Yang et al.*, 2014].

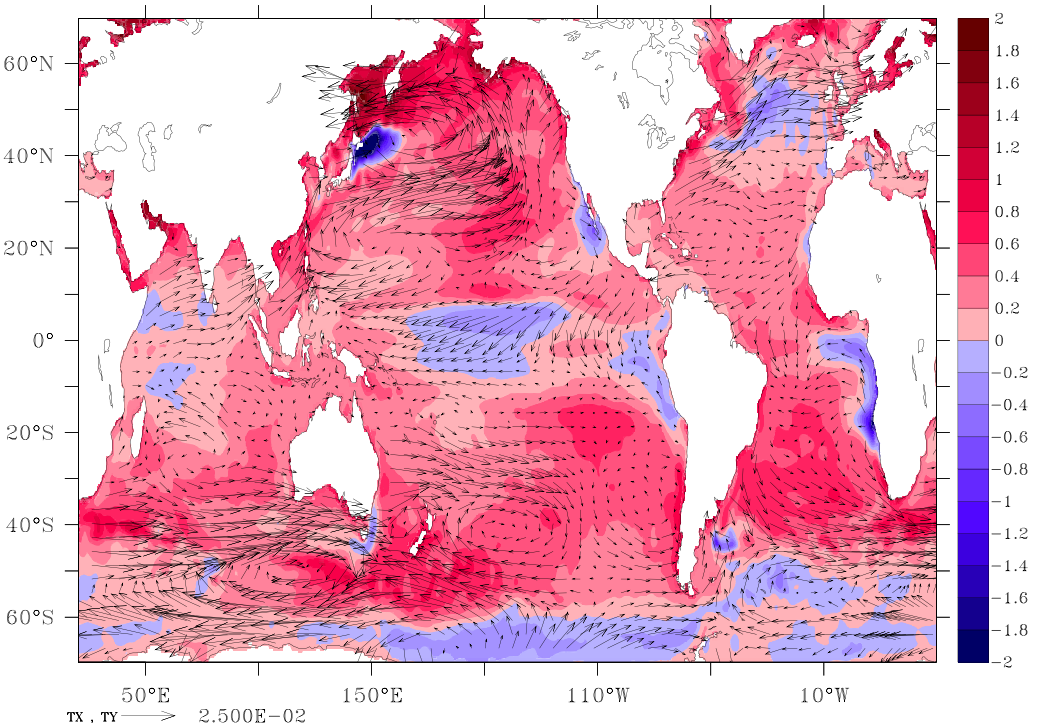

Figure 11. The ensemble mean SST tendency (shaded) in °C Century^{-1} and wind stress tendency (vectors) in N m^{-2} Century^{-1} from 1815 through 2013.

To investigate some of the possible physical mechanisms associated with the secular changes in SST seen in EOFs 1-3, we present the tendencies of SST and surface wind stress for the reanalysis period over the global oceans in Figure 11 with vectors that represent the change in zonal and meridional stress in N m^{-2} century^{-1}. In the Pacific Ocean, there is cyclonic flow centered near 45°N and 45°S, broadly consistent with an atmospheric circulation that has been shifted toward the equator. In the North Pacific Ocean, the cyclonic flow generates a region of cooling in the Kuroshio extension region. In the tropics, there are increasing easterly trade winds in the central and western Pacific, and weakening easterly trade winds in the eastern Pacific. This divergence gives rise to the cooling region in the central and western Pacific Ocean [*Yang et al.*, 2014]. In the tropical Atlantic Ocean, there are stronger trade winds near the coast of Africa, giving rise to the cooling tendency apparent there. In the North Atlantic Ocean, there are stronger midlatitude westerlies that accompany a region of cooling in the central region of the basin. Throughout much of the Southern Ocean (poleward of 60°S), the tendency is easterly, driving cooling near the coast of Antarctica.

The second EOF (shown in Figure 10b) accounts for 15% of the variance and has considerable longitudinal structure in the Pacific and Atlantic Oceans, and in the Southern Ocean. This variability has largely multidecadal time scales, and appears to be consistent with global representations of the Atlantic Multi-decadal Oscillation [e.g., *Newman*, 2013]. One advantage of an ocean reanalysis is that it provides an estimate of the 3-dimensional fields of temperature and salinity governed by ocean dynamics. To better understand the SST changes described by the EOF analysis, we computed the meridional stream function for the Atlantic Ocean. The spatial average of reconstructed SST using the second EOF from 90°W to 20°E and from 35°N to 80°N (the region of greatest warming in the North Atlantic Ocean) is plotted in Figure 12 as a black line. Plotted as a red line is the North Atlantic maximum of the stream function. The second EOF of SST is correlated with the overturning stream function with a correlation coefficient of 0.69. Inspection of Figure 12 suggests that there is a lag between the two time series. Interestingly, the correlation rises to 0.84 if the stream function is advanced (implying that temperature leads stream function) by 9 years. Wind stress regressed onto the principal component time series associated with the second EOF of SST is shown in Figure 13. The winds show a weakening of the atmospheric circulation over much of the Atlantic Ocean, consistent with a weakened equator-to-pole temperature gradient when the second EOF is in the positive state shown in Figure 10b.

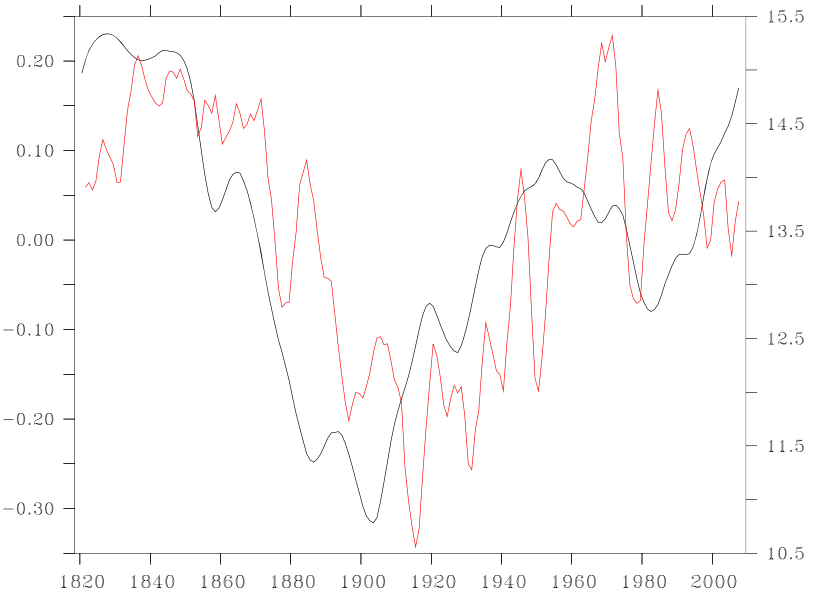

Figure 12. SST from the second EOF averaged from 90°W to 20°E and from 35°N to 80°N in °C plotted as a black line (left axis). Also shown is the maximum of the stream function in the North Atlantic Ocean in Sverdrups is shown as a red line (right axis). Both time series have been smoothed with a 5 year box-car average.

The third EOF explains just 7% of the variance and has a spatial structure that is reminiscent of ENSO (El Nino Southern Oscillation) and is shown in Figure 10c. The temporal structure of this EOF is consistent with the fact that ENSO events were strong in the late 19th and early 20th Centuries and again in the late 20th Century, with weak ENSO from the 1920s through the 1950s (with a brief exception for the 1941–1943 El Niño) [*Giese and Ray*, 2011]. *Compo and Sardeshmukh* [2010] demonstrated that this pattern's structure

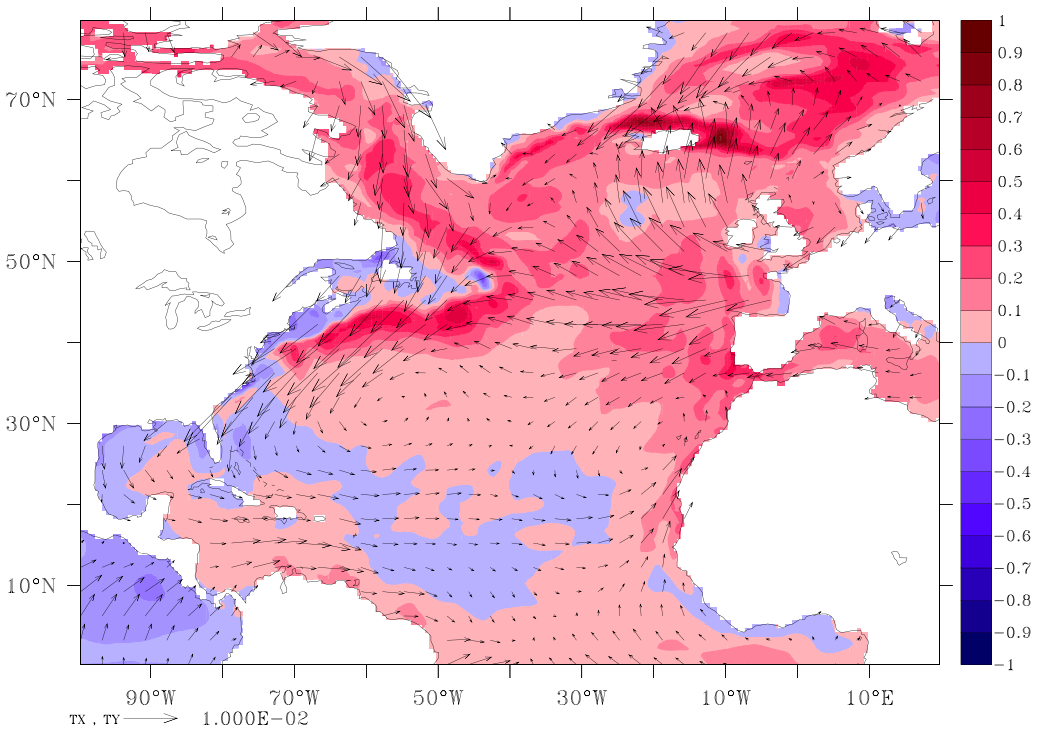

Figure 13. Surface wind stress projected onto the temporal component of the second EOF of SST. Shading shows the second EOF of SST, as in Figure 10b.

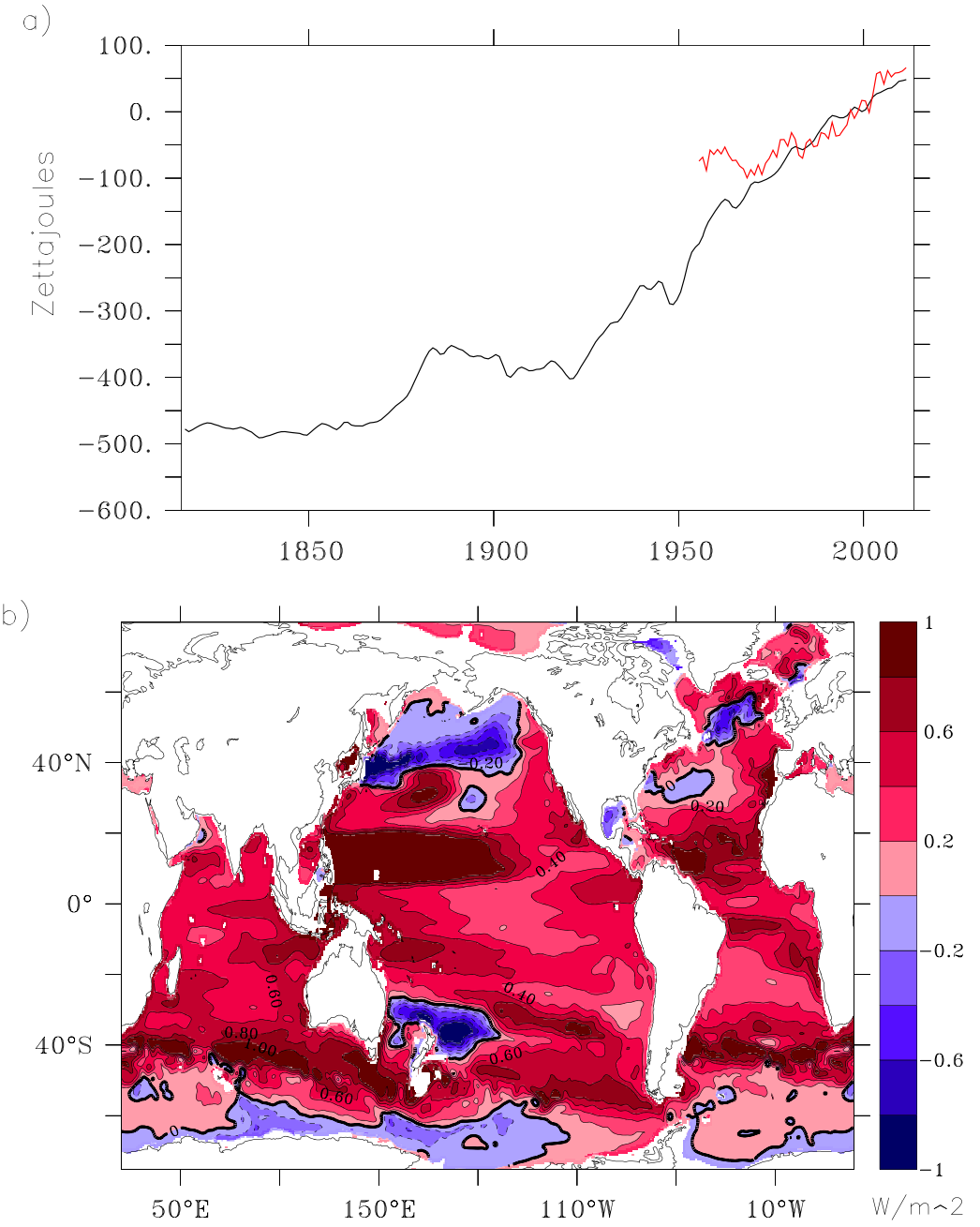

Figure 14. (a) Heat content from the surface to 700 m in zettajoules (10^{21} J) integrated globally for the SODAsi.3 ensemble mean (black line). The data have been smoothed with a 23 month Parzen filter. Heat content 0–700 m from *Levitus et al.* [2012] is shown as a red line. Both time series are adjusted to have zero mean from 1984 to 2013. (b) The time rate of change of heat content in W m^{-2} averaged from 1815 through 2013.

reflects a combination of ENSO-related and ENSO-unrelated decadal variability. Interestingly, this pattern also shows what has been termed a "climate shift" in 1976 [*Giese et al.*, 2002], with a prominent warming in the tropical Pacific Ocean and cooling in the North and South Pacific Oceans that have been related to variations associated with the Pacific Decadal Oscillation [*Newman et al.*, 2016]. There also appears to be a shift to a cooler east Pacific SST just after 1900.

The reanalysis can also be used to investigate subsurface quantities. An important measure of ocean climate is the heat content of the upper ocean [*Levitus et al.*, 2012]. Figure 14a shows the temporal evolution of globally integrated heat content of the upper 700 m in zettajoules (10^{21} joules) from the ensemble mean of SODAsi.3. Also shown is heat content of the upper 700 m as estimated by *Levitus et al.* [2012] using

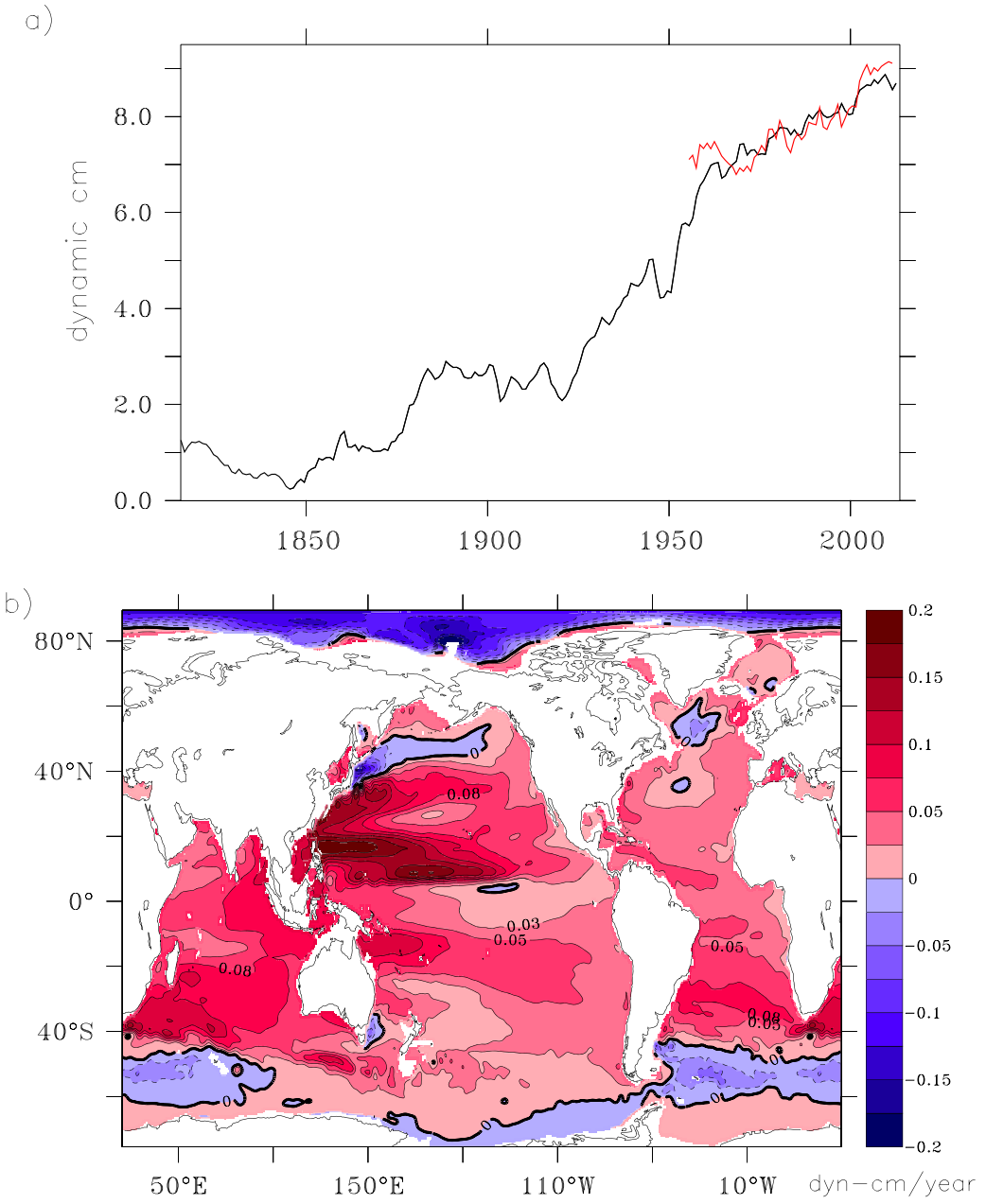

Figure 15. (a) Dynamic height calculated relative to 1000 m in dyn-cm averaged globally. The data have been smoothed with a 23 month Parzen filter. The global average thermosteric height anomaly from 0 to 700 m produced by *Levitus et al.* [2012] is shown as a red line. (b) The time rate of change of dynamic height in dyn-cm year^{-1} averaged from 1815 through 2013.

hydrographic observations. This comparison provides an independent check on the reanalysis, because hydrographic observations are not assimilated in SODAsi. Both time series have been adjusted to have zero mean for the last 30 years of the record, from 1984 to 2013. The reanalysis shows a nearly monotonic increase from about 1920 to the present, with relatively brief periods of decreasing heat content in the late 1940s and early 1960s. Interestingly, these brief periods are much shorter than the cooling of SST from the mid-1940s through the mid-1970s apparent in Figure 9. Heat content from SODAsi.3 agrees well with heat content estimated by *Levitus et al.* [2012] from about 1980 onward. While there is greater discrepancy before 1980, it should be noted that there are relatively few hydrographic observations during this period, and before the introduction of the XBT in the late 1960s, they are almost all confined to the upper part of the water column (above 200 m) [*Carton and Giese*, 2008].

The time derivative of heat content gives the flux of heat required for the temperature change. The spatial pattern of this flux in W m^{-2}, averaged from 1815 to 2013, is shown in Figure 14b. The flux required to account for changes of heat content is large in the western Pacific and Indian Oceans, and throughout much of the Atlantic Ocean. The largest values, at about 1 W m^{-2} occur in the west Pacific Ocean just north of the equator. There are regions of negative flux as well, in the Kuroshio extension region, in the central North Atlantic Ocean, and in the region around Antarctica that also has cooling SST. Averaging globally gives the total amount of heat transferred from the atmosphere to the ocean to account for this net ocean warming. Because much of the heat content change occurs after about 1920, these fluxes are considerably larger (and with slightly different spatial patterns) when calculated from 1920 to 2013. The average flux needed to account for the global change in heat content to 700 m from 1920 to 2013 is 0.47 W m^{-2}. This value is quite consistent with the 0.42 W m^{-2} reported in the IPCC AR5 as being required to account for heat content changes from 1971 to 2010 as calculated using in situ observations [*Rhein et al*., 2013].

The spatial variations in heat flux arise in part from changes in ocean circulation and the subsurface redistribution of heat. In particular, the changes in the tropical Pacific Ocean are suggestive of a dynamic redistribution of heat, broadly consistent with an intensified Walker circulation over the century [*L'Heureux et al*., 2013, *Sandeep et al*., 2014, *Yang et al*., 2014]. The largest wind stress change (Figure 11) occurs in the Northern Hemisphere, and in particular the North Pacific Ocean. The North Pacific wind stress trend is mostly cyclonic, generally consistent with a southward migration of the Hadley cell circulation [*Giese and Carton*, 1999]. South of this cyclonic circulation is a region of weaker anticyclonic circulation. In the North Atlantic Ocean, there are mostly enhanced westerlies extending across the basin from about 30°N to 60°N. To the south there is weaker anticyclonic circulation, similar to the structure in the Pacific Ocean.

In the tropical Pacific Ocean, there are enhanced easterlies (Figure 11) and in the eastern Pacific Ocean there are weakened southeast trade winds, giving a surface wind divergence in the central Pacific Ocean at around 130°W. *Yang et al*. [2014] identified this divergence as being responsible for the cooling tendency in this region. Across the Southern Ocean, there is cyclonic flow in all three basins, consistent with the warming north of 60°S and cooling south of 60°S captured by the first EOF of SST (see Figure 10a).

Given the importance of temperature to sea level change, we expect changes in heat content to correspond to regions of sea level change. Dynamic height relative to 1000 m is shown in Figure 15 in dynamic centimeters (dyn-cm). The globally averaged dynamic height is presented in Figure 15a and, as with heat content, shows an increase over the reanalysis period with an overall increase of about 9.0 dyn-cm, giving an average rate of about 0.45 mm yr^{-1}, although much of this change occurs after 1920. After 1920, there is a slightly stronger height increase from 1920 to about 1960, with a slightly weaker trend from 1960 to 2011. Using the period from 1955 to 2010 gives a rate of increase of 0.55 mm yr^{-1}, quite similar to the value of 0.54 mm yr^{-1} for thermosteric sea level rise reported by *Levitus et al*. [2012].

The spatial pattern of dynamic height tendency is shown in Figure 15b. It is similar, but not identical to the change of heat content presented in Figure 14b. The west Pacific and Indian Ocean have prominent dynamic height increases, while much of the eastern Pacific Ocean has weaker trends and the high latitude Southern Ocean shows a decreasing dynamic height tendency. Two regions where heat content and dynamic height are distinctly different are in the Arctic and far North Atlantic Oceans. In the North Atlantic Ocean, changes in dynamic height are relatively modest, whereas there are large changes in heat content suggesting that there are important contributions from salinity to dynamic height. In the Arctic, there is decreasing dynamic height but weakly increasing heat content, however we do not expect the reanalysis to perform well in this region because the model lacks an active sea-ice component.

4. Summary and Conclusions

We present results from 18 member (SODAsi.2) and 8 member (SODAsi.3) ensembles of ocean reanalyses with SODAsi.3 spanning the period from 1815 to 2013. The SODAsi ensemble members were generated using ensembles of 20CR surface boundary conditions and a "loosely-coupled" iterative coupling between the SODA and 20CR systems. The coupled system is particularly important for the SODAsi reanalyses because although there are few ocean observations throughout most of the 1800s, there are atmospheric

surface pressure observations in the early part of the record [*Cram et al*., 2015]. The ocean reanalyses draw information about SST from these surface pressure observations via the momentum and surface heat fluxes determined from the atmospheric reanalyses. The loosely coupled system lessens, but does not eliminate, the problem of the time dependent density of SST observations.

Using ensemble member forcing corrects an important bias associated with using ensemble mean forcing. During periods of few observations, the "weather noise" is averaged out of the ensemble mean, whereas during periods of dense observations the weather noise is correlated across the ensemble members and so is not averaged out. This can appear as a time dependent change in weather intensity as the number of observations increases [e.g., *Wang et al*. 2013, 2014].

A second source of bias addressed by SODAsi has to do with the time dependent nature of observations in the ocean. *Yang and Giese* [2013] report that introducing hydrographic observations in the 1960s leads to increasing circulation strength, and introduces a spurious trend that is difficult to separate from climate variability. This strengthening arises because the introduction of subsurface observations tightens the density gradients and thus acts to increase current speed. Because SODAsi uses only sea surface temperature observations from ICOADS 2.5, the bias due to introducing hydrographic observations is eliminated. The only temperature observations that are assimilated in this new reanalysis are the SST data in the ICOADS 2.5 data set. It should be noted that, by excluding hydrographic observations, SODAsi.3 is not as well constrained in modern times (post 1950s) as other ocean reanalyses that use the full complement of observations. Instead, SODAsi.3 is intended for researchers who require a continuous record over a 200 year period.

The SODAsi.3 SST fields show a wide range of variability on time scales that range from interannual to decadal to trends. There is overall agreement between the reanalyses and previously published SST estimates from reconstructions, however there are also some important differences. There is good agreement in a pronounced trend in SST in both SODAsi.3 and reconstructed SST from the early 1900s to the present. SODAsi.3 shows that the spatial pattern of this trend has increasing temperature throughout the global oceans, except for a few regions of cooling. These regions include the central tropical Pacific and eastern tropical Atlantic Oceans, the region around Antarctica, and in the Gulf Stream and Kuroshio extension regions.

An EOF analysis of SST shows that in addition to long-term trends there is considerable multidecadal variability. In the North Atlantic, the multidecadal variability varies by about 0.5°C. The second EOF structure is highly correlated to the meridional overturning stream function, which varies in strength from about 15 Sv to about 11 Sv. Interestingly, the correlation increases when a lag for the stream function is taken into consideration. The maximum correlation (0.84) occurs when the stream function is shifted forward by 9 years. These results are relevant to two recently published studies of North Atlantic SST and the meridional overturning stream function. *Rahmstorf et al*. [2015] find that a region of cooling amid overall warming in the North Atlantic Ocean is related to a slowdown in the meridional overturning stream function. Although our results also show a region of cooling amid an overall warming trend, we do not see evidence of an overall trend of the overturning stream function. Instead, variations of the overturning stream function in SODAsi.3 are connected to the second EOF of SST. However changes in the stream function lag changes in SST by about 9 years. This appears to corroborate the findings of *Clement et al*. [2015] who show that in their coupled model, changes in North Atlantic warming do not require a concomitant change in ocean circulation. Instead, they propose that changes in circulation respond to changes in SST, which is what we find as well. There is an ongoing discussion of the relationship between North Atlantic circulation and decadal SST variations [*Zhang et al*., 2016; *Clement et al*., 2016; *O'Reilly et al*., 2016]. Historical ocean reanalyses, such as the one presented here, may help us to understand the mechanisms that determine low frequency SST variability.

One of the most important advantages of having a reanalysis over an SST reconstruction is that the reanalysis has a full 3-dimensional representation of the ocean state, including an estimate of the circulation that is dynamically balanced with the temperature and salinity fields. The 3-dimensional fields allow us to explore climate change in the subsurface ocean. The ensemble average of dynamic height relative to 1000 m and heat content integrated to 700 m agree well with values from an independent analysis that uses only hydrographic observations. Both dynamic height and heat content show that their global averages increase

nearly linearly from about 1920 to the present. The heat content increase requires a net flux of heat of about 0.4 W m^{-2}.

The sensitivity of the ocean to ensemble forcing from the atmosphere raises the issue of how sensitive would an atmosphere reanalysis be to ensemble forcing for SST. The results presented here suggest that a similar study for the atmosphere could be instructive in understanding air-sea interaction in the context of data assimilation. The logical extension of this study is that a fully coupled climate model with data assimilation would result in a state estimate that better represents the coupled nature of the climate system than separate reanalyses of the individual components.

Acknowledgments
Support for B.S.G. and H.F.S. was provided by NOAA grant NA10OAR4310201 and NSF grant 1049075. We are grateful to Philip Brohan, who provided the Hadley Centre bucket corrections, Jeff Whitaker, who worked to develop the 20CR Ensemble Filter, and Chesley McColl, Xungang Yin, and Nobuki Matsui, who prepared versions of the ISPD. The ISPD version 4 benefited from new contributions from previous contributors to the ACRE initiative led by R. Allan of the UK Met Office, and from contributions courtesy of L. Alexander of the University of New South Wales; P. Brohan of the UK Met Office, K. Wood of JISAO, and the volunteers of Oldweather.org; M. Benoy and volunteers of the Australian Meteorological Association; A. Dawson of the University of Aberdeen; D. Efthmymiadis of the Universitat Rovira I Virgili; A. Kaplan of the Lamont Doherty Earth Observatory; A. Kijazi of the Tanzania Meteorological Agency; R. Kocen of the University of Bern; H. Maechel of the DWD; A. Moberg of Stockholm University; R. Przybylak of Nicolaus Copernicus University; C. Pudmenzky of the University of Southern Queensland and the volunteers of WeatherDetective.org; C. Rakich of the Australian Bureau of Meteorology; V. Slonosky and volunteers of the Canadian Volunteer Data Rescue Project; and A. Tsikerdekis of the University of Giessen. The Twentieth Century Reanalysis Project and the International Surface Pressure Databank used resources of the National Energy Research Scientific Computing Center managed by Lawrence Berkeley National Laboratory and of the Oak Ridge Leadership Computing Facility at Oak Ridge National Laboratory, which are supported by the Office of Science of the U.S. Department of Energy under contract DE-AC02-05CH11231 and contract DE-AC05-00OR22725, respectively. Support for the Twentieth Century Reanalysis Project data set and the International Surface Pressure Databank is provided by the U.S. Department of Energy, Office of Science Innovative and Novel Computational Impact on Theory and Experiment (DOE INCITE) program, and Office of Biological and Environmental Research (BER), and by the National Oceanic and Atmospheric Administration Climate Program Office. The data used are available at http://soda.tamu.edu.

References

Allan, R., P. Brohan, G. P. Compo, R. Stone, J. Luterbacher, and S. Brönnimann (2011), The international atmospheric circulation reconstructions over the earth (ACRE) initiative, *Bull. Am. Meteorol. Soc.*, *92*, 1421–1425.

Brönnimann S., G. P. Compo, R. Allan, W. Adam, and R. Spadin (2011), Early ship-based upper-air data and comparison with the Twentieth Century Reanalysis, *Clim. Past*, *7*, 265–276, doi:10.5194/cp-7-265-2011.

Brönnimann, S., A. N. Grant, G. P. Compo, T. Ewen, T. Griesser, A. M. Fischer, M. Schraner, and A. Stickler (2012), A multi-data set comparison of the vertical structure of temperature variability and change over the Arctic during the past 100 years, *Clim. Dyn.*, *39*, 1577–1598, doi:10.1007/s00382-012-1291-6.

Brugnara, Y., et al. (2015), A collection of sub-daily pressure and temperature observations for the early instrumental period with a focus on the "year without a summer" 1816, *Clim. Past*, *11*, 1027–1047, doi:10.5194/cp-11-1027-2015.

Carton, J. A., and B. S. Giese (2008), A reanalysis of ocean climate using simple ocean data assimilation (SODA), *Mon. Weather Rev.*, *136*, 2999–3017, doi:10.1175/2007MWR1978.1.

Carton, J. A., H. F. Seidel, and B. S. Giese (2012), Detecting historical ocean climate variability, *J. Geophys. Res.*, *117*, C02023, doi:10.1029/2011JC007401.

Clement, A., K. Bellomo, L. N. Murphy, M. A. Cane, T. Mauritsen., G. Rädel, and B. Stevens (2015), The Atlantic multidecadal oscillation without a role for ocean circulation, *Science*, *350*(6258), 320–324, doi:10.1126/science.aab3980.

Clement, A., M. A. Cane., L. N. Murphy, K. Bellomo., T.Mauritsen, B. Stevens (2016), Response to comment on "The Atlantic Multidecadal Oscillation without a role for ocean circulation," *Science*, *352*, 1527, doi:10.1126/science.aaf2575.

Compo, G. P., and P. D. Sardeshmukh (2010), Removing ENSO-related variations from the climate record, *J. Clim.*, *23*, 1957–1978, doi:10.1175/2009JCLI2735.1.

Compo, G. P., J. S. Whitaker, and P. D. Sardeshmukh (2006), Feasibility of a 100-year reanalysis using only surface pressure data. *Bull. Am. Meteorol. Soc.*, *87*, 175–190, doi:10.1175/BAMS-87-2-175.

Compo G. P. et al. (2011), The twentieth century reanalysis project, *Q. J. R. Meteorol. Soc.*, *137*, 1–28, doi:10.1002/qj.776.

Compo, G. P., P. D. Sardeshmukh, J. S. Whitaker, P. Brohan, P. D. Jones, and C. McColl (2013), Independent confirmation of global land warming without the use of station temperatures, *Geophys. Res. Lett.*, *40*, 3170–3174, doi:10.1002/grl.50425.

Cram, T., et al. (2015), The International Surface Pressure Databank version 2, *Geosci. Data J.*, *2*, 31–46, doi:10.1002/gdj3.25.

Crowley, T., and M. Unterman, (2013), Technical details concerning development of a 1200 year proxy index for global volcanism, *Earth Syst. Sci. Data*, *5*, 187–197.

Daley, R. (1991), *Atmospheric Data Assimilation*, 457 pp., Cambridge Univ. Press, Cambridge.

Dee, D. P., et al., (2011), The ERA-Interim reanalysis: Configuration and performance of the data assimilation system, *Q. J. R. Meteorol. Soc.*, *137*, 553–597, doi:10.1002/qj.828.

Giese, B. S., and J. A. Carton (1999), Interannual and decadal variability in the tropical and midlatitude Pacific Ocean, *J. Clim.*, *12*, 3402–3418.

Giese, B. S., and D. E. Harrison (1990), Aspects of the Kelvin wave response to episodic wind forcing, *J. Geophys. Res.*, *95*, 7289–7312, doi:10.1029/JC095iC05p07289.

Giese, B. S., and S. Ray (2011), El Niño variability in simple ocean data assimilation (SODA), 1871–2008, *J. Geophys. Res.*, *116*, C02024, doi:10.1029/2010JC006695.

Giese, B. S., S. C. Urizar, and N. S. Fučkar (2002), Southern hemisphere origins of the 1976 climate shift, *Geophys. Res. Lett.*, *29*(2), 1014, doi:10.1029/2001GL013268.

Giese B. S., G. P. Compo, N. C. Slowey, P. D. Sardeshmukh, J. A. Carton, S. Ray, and J. S. Whitaker (2010), The 1918/1919 El Niño. *Bull. Am. Meteorol. Soc.*, *91*, 177–183, doi:10.1175/2009BAMS2903.

Greve, P., B. Orlowsky, B. Mueller, J. Sheffield, M. Reichstein, and S. I., Seneviratne (2014), Global assessment of trends in wetting and drying over land, *Nat. Geosci.*, *7*, 716–721.

Hirahara, S., M. Ishii, and Y. Fukuda (2014), Centennial-scale sea surface temperature analysis and its uncertainty, *J. Clim.*, *27*, 57–75, doi:10.1175/JCLI-D-12-00837.1.

Huang, B., V. F. Banzon, E. Freeman, J. Lawrimore, W. Liu, T. C. Peterson, T. M. Smith, P. W. Thorne, S. D. Woodruff, and H.-M. Zhang (2015), Extended reconstructed sea surface temperature version 4 (ERSST.v4): Part I. Upgrades and intercomparisons, *J. Clim.*, *28*, 911–930, doi:10.1175/JCLI-D-14-00006.1.

Jones, P. W. (1999), First and second-order conservative remapping schemes for grids in spherical coordinates, *Mon. Weather Rev.*, *127*, 2204–2210.

Kalnay, E. (2003), *Atmospheric Modelling*, Data Assimilation, and Prediction, 341 pp., Cambridge Univ. Press, Cambridge.

Kaplan, A., M. A. Cane, Y. Kushnir, A. C. Clement, M. B. Blumenthal, and B. Rajagopalan (1998), Analyses of global sea surface temperature 1856–1991, *J. Geophys. Res.*, *103*, 18,567–18,589.

Kent, E. C., S. Fangohr, and D. I. Berry (2012), A comparative assessment of monthly mean wind speed products over the global ocean, *Int. J. Climatol.*, 11, 2520–2541, doi:10.1002/joc.3606.

Kiladis, G. N., and H. F. Diaz (1986), An analysis of the 1877–78 ENSO episode and comparison with 1982–83, *Mon. Weather Rev.*, *114*, 1035–1047, doi:10.1175/1520-0493(1986)114 < 1035:AAOTEE>2.0.CO;2.

Levitus, S., et al. (2012), World ocean heat content and thermosteric sea level change (0–2000 m), 1955–2010, *Geophys. Res. Lett.*, *39*, L10603, doi:10.1029/2012GL051106.

L'Heureux M. L., S. Lee, and B. Lyon (2013), Recent multidecadal strengthening of the Walker Circulation across the tropical Pacific, *Nat. Clim. Change*, *3*(6), 571–576, doi:10.1038/nclimate1840.

Meehl, G. A., et al. (2007), Global climate projections, in *Climate Change 2007: the Physical Science Basis. Contribution of Working Group I to the Fourth Assessment Report of the Intergovernmental Panel on Climate Change*, pp.747–846, edited by S. Solomon et al., Cambridge Univ. Press, Cambridge.

Newman, M., (2013), An empirical benchmark for decadal forecasts of global surface temperature anomalies, *J. Clim.*, *26*, 5260–5269, doi: 10.1175/JCLI-D-12-00590.1.

Newman, M, et al. (2016), The Pacific decadal oscillation, revisited, *J. Clim.*, *29*(12), 4399–4427, doi:10.1175/JCLI-D-15-0508.1.

O'Reilly, C. H., M. Huber, T. Woollings, and L. Zanna (2016), The signature of low-frequency oceanic forcing in the Atlantic Multidecadal Oscillation, *Geophys. Res. Lett.*, *43*, 2810–2818, doi:10.1002/2016GL067925.

Quinn, W. H., V. T. Neal, and S. E. Antunez de Mayolo (1987), El Niño occurrences over the past four and a half centuries, *J. Geophys. Res.*, *92*, 14,449–14,461.

Rahmstorf, S., J. E. Box, G. Feulner, M. E. Mann, A. Robinson, S. Rutherford, and E. J. Schaffernicht (2015), Exceptional twentieth-century slowdown in Atlantic Ocean overturning circulation, *Nat. Clim. Change*, *5*, 475–480, doi:10.1038/nclimate2554.

Ray, S., and B. S. Giese (2012), Historical changes in El Niño and La Niña characteristics in an ocean reanalysis, *J. Geophys. Res.*, *117*, C11007, doi:10.1029/2012JC008031.

Rayner, N. A., D. E. Parker, E. B. Horton, C. K. Folland, L. V. Alexander, D. P. Powell, E. C. Kent, and A. Kaplan (2003), Global analyses of sea surface temperature, sea ice, and night marine air temperature since the late nineteenth century, *J. Geophys. Res*, *108*(D14), 4407, doi: 10.1029/2002JD002670.

Reynolds, R. W., T. M. Smith, C. Liu, D. B. Chelton, K. S. Casey, and M. G. Schlax (2007), Daily high-resolution-blended analyses for sea surface temperature, *J. Clim.*, *20*, 5473–5496.

Rhein, M. et al. (2013), Observations: Ocean, in *Climate Change 2013: The Physical Science Basis. Contribution of Working Group I to the Fifth Assessment Report of the Intergovernmental Panel on Climate Change*. edited by T. F. Stocker et al., Cambridge Univ. Press, Cambridge, U. K.

Sandeep, S., F. Stordal, P. D. Sardeshmukh, and G. P. Compo (2014), Pacific walker circulation variability in coupled and uncoupled climate models. *Clim. Dyn.*, *43*, 103–117, doi:10.1007/s00382-014-2135-3.

Smith, R. D., J. K. Dukowicz, and R. C. Malone (1992), Parallel ocean general circulation modeling, *Physica D*, *60*, 38–61.

Stickler, A., S. Brönnimann, M. A. Valente, J. Bethke, A. Sterin, S. Jourdain, E. Roucaute, M. V. Vasquez, D. A. Reyes, R. Allan, and D. Dee (2014), ERA-CLIM: Historical surface and upper-air data for future reanalyses, *Bull. Am. Meteorol. Soc.*, *95*, 1419–1430.

Wang, X. L., Y. Feng, G. P. Compo, V. R. Swail, F. W. Zwiers, R. J. Allan, and P. D. Sardeshmukh (2013), Trends and low frequency variability of extra-tropical cyclone activity in the ensemble of twentieth century reanalysis, *Clim. Dyn.*, *40*, 2775–2800, doi:10.1007/s00382-012-1450-9.

Wang, X. L., Y. Feng, G. P. Compo, F. W. Zwiers, R. J. Allan, V. R. Swail, and P. D. Sardeshmukh (2014), Is the storminess in the twentieth century reanalysis really inconsistent with observations? A reply to the comment by Krueger et al. (2013b), *Clim. Dyn.*, *42*, 1113–1125, doi: 10.1007/s00382-013-1828-3.

Whitaker, J. S. and T. M. Hamill (2002), Ensemble data assimilation without perturbed observations, *Mon. Weather Rev.*, *130*, 1913–1924, doi:10.1175/1520-0493(2002)130≤1913:EDAWPO≥2.0.CO;2.

Whitaker, J. S., G. P. Compo, X. Wei, and T. M. Hamill (2004), Reanalysis without radiosondes using ensemble data assimilation, *Mon. Weather Rev.*, *132*, 1190–1200.

Woodruff, S. D., et al. (2010), ICOADS Release 2.5: Extensions and enhancements to the surface marine meteorological archive, *Int. J. Climatol.*, *31*, 951–967, doi:10.1002/joc.2103.

Yang, C., and B. S. Giese (2013), El Niño Southern Oscillation in an ensemble ocean reanalysis and coupled climate models, *J. Geophys. Res. Oceans*, *118*, 4052–4071, doi:10.1002/jgrc.20284.

Yang, C., B. S. Giese, and L. Wu (2014), Ocean dynamics and tropical Pacific climate change in ocean reanalyses and coupled climate models, *J. Geophys. Res. Oceans*, *119*, 7066–7077, doi:10.1002/2014JC009979.

Zhang, R., R. Sutton, G. Danabasoglu, T. L. Delworth, W. M. Kim, J. Robson, and S. G. Yeager (2016), Comment on "The Atlantic Multidecadal Oscillation without a role for ocean circulation," *Science*, *352*, 1527, doi:10.1126/science.aaf1660.